# Total Internal Reflection Peak Force Infrared Microscopy

Haomin Wang[1], Le Wang[1], Eli Janzen[2], James H. Edgar[2], and Xiaoji G. Xu[1]*

[1]Department of Chemistry, Lehigh University, Bethlehem, PA 18015, USA.

[2]Tim Taylor Department of Chemical Engineering, Kansas State University, Durland Hall, Manhattan, KS 66506, USA.

*Corresponding email: xgx214@lehigh.edu

**ABSTRACT:** Total internal reflection (TIR) infrared spectroscopy is a convenient measurement tool for collecting spectra for chemical identification. However, TIR infrared microscopy lacks high spatial resolution due to the optical diffraction limit and difficulty to preserve a high-quality wave front for focus. In this article, we present the peak force infrared microscopy in the TIR geometry to achieve a 10 nm spatial resolution. Instead of optical detection, photothermal responses of the sample are collected in the peak force tapping mode of atomic force microscopy. We demonstrate the technique on two representative samples: structured polymers for soft matters and a hexagonal boron nitride flake for two-dimensional materials. As an extension of the apparatus, we also demonstrate nano infrared imaging with the TIR excitation for photo-induced force microscopy. The combination of TIR geometry with nano-infrared microscopies simplifies the optical alignment, providing alternative instrument-designing principles for atomic force microscopy-based infrared microscopy.

## Introduction

Infrared radiation directly couples to the vibrational modes of molecules that are characteristic of functional groups and their chemical environment. Infrared spectroscopy measures the vibrational absorption of the sample and is widely used as a chemical identification tool. A popular implementation of infrared spectroscopy is through the measurement of the attenuated total internal reflection of infrared radiation by a sample, which leads to the method of attenuated total internal reflection infrared (ATR-IR) spectroscopy. ATR-IR has the advantage of easy sample preparation over the regular transmission-type infrared spectroscopy by avoiding creating pellets. ATR-IR has been widely applied in a range of areas, including chemically identifying soft and rigid materials,[1-3] imaging biological and pharmaceutical samples,[4-6] and studying catalytic interfaces.[7-9] However, ATR-IR methods have an intrinsic limitation: the optical diffraction limit sets a physical boundary on the spatial resolution to one half of the wavelength.[10] In practice, the total internal reflection prism also causes wave front distortion in the optical delivery, and even the diffraction-limited spatial resolution is challenging to attain for ATR-IR microscopy. So far, the best spatial resolution of ATR-IR microscopy is only 3-4 μm.[11, 12] On the other hand, a high spatial resolution is instrumental for material research, because not all samples are homogeneous at the micro- to the nanoscale.

The optical diffraction limit on the spatial resolution of ATR-IR microscopy can be bypassed by implementing action-based nanoscopy or scattering-type near-field optical microscopy (s-SNOM). In action-based nanoscopies, the laser-induced photothermal response resulting from infrared absorptions is mechanically detected with a sharp tip of the atomic force microscope (AFM).[13-15] In s-SNOM, the scattered light from the sharp metallic tip is detected, and the scattering signal is based on local tip-sample near-field interactions.[16] The evanescent field generated from the total internal reflection (TIR) has been utilized in s-SNOM to achieve sub-wavelength nano imaging.[17, 18] Recently, s-SNOM with different TIR geometries was performed in water with 30-80 nm spatial resolution and chemical sensitivity.[19, 20] Because amplitude of the scattering signal from s-SNOM depends on the polarizability of the

tip-sample region rather than the absorption, multiple interferometric detection schemes have been developed to recover the phase or the imaginary part the near-field signal, [21-23] which corresponds to the infrared absorptions. On the other hand, photothermal signal from action-based nanoscopies is directly comparable to conventional infrared signatures of samples.[14] The development of the TIR geometry in the photothermal induced resonance (PTIR) brought the spatial resolution down to 50-100 nm in mid-infrared, and a 20-nm spatial resolution at a light wavelength of 725 nm was demonstrated.[24] The detection mechanism in PTIR is based on the detection of the contact resonance of the cantilever in the contact mode of AFM. However, the contact mode AFM is prone to damaging the sample surface, as the lateral force between the AFM tip and the sample can scratch the sample surface during the raster scan. A more sample friendly AFM mode is needed to be combined with the TIR geometry for nanoscale infrared imaging. Such requirement is fulfilled by using tapping mode in photoinduced force microscopy (PiFM)[25] or peak force tapping mode in peak force infrared (PFIR) microscopy. [26] PFIR microscopy and PiFM were developed based on the geometry of side illumination, i.e., the infrared light arriving at the tip from the side. The combination of the the TIR geometry with these non-contact mode AFM-IR methods has not been implemented.

In this manuscript, we demonstrate the combination of the TIR geometry with the PFIR microscopy as well as the PiFM. A high spatial resolution of 10 nm is achieved for total internal reflection peak force infrared (TIR-PFIR) microscopy. The demonstration of TIR-PFIR proves that the evanescent field formed from TIR of a Ge prism is capable of generating detectable photothermal expansions, although the AFM tip is in intermittent contact with the sample. Vulnerabilities of the contact mode AFM of the PTIR microscopy in TIR geometry are also avoided. Finite-difference time-domain (FDTD) simulation results also suggest the evanescent field formed in the TIR configuration provides a significantly larger field enhancement factor than the direct side illumination configuration when the tip and sample are close. Therefore, the requirement for a high numerical aperture focusing unit is lessened. A large focus spot can be used for the TIR-PFIR, which translates into simplification of the alignment procedure and maintenance for the apparatus.

**Experimental Section**

**Implementation of TIR-PFIR.** When the incident angle is larger than the critical angle, an optical beam undergoes TIR by a prism, and an evanescent field is established at the interface.[27] The electrical field of the evanescent field is amplified compared with the intensity of the incident radiation.[27, 28] If a metal-coated AFM tip is present within the evanescent field, an even larger field enhancement is expected, similar to the field enhancement brought by plasmonic nanoparticles.[29] Figure 1a illustrates the FDTD simulation of the field enhancement by the evanescent field from a Ge prism; the field is enhanced 5400 times on the Ge surface beneath a Au tip with a 30-nm end radius. In contrast, in the direct illumination configuration, the Au-Ge surface only provides an enhancement factor of 240 from free-space side illumination (Figure 1b). The additional field enhancement from the TIR means a smaller incident photon intensity can be used to achieve the same photothermal expansion effect, compared with free-space illumination. Given the same laser power, the utilization of TIR means that the laser beam can be focused less tight than the free-space beam focus, which indicates the alignment for the TIR geometry is less stringent than that of the free-space delivery.

Figure 1c illustrates the design of the TIR-PFIR apparatus. The TIR condition is created by placing the AFM tip on top of a Ge prism mounted on a flexure piezoelectric scanner stage. The AFM (Bioscope Catalyst, Bruker) is operated by an AFM controller (Nanoscope V, Bruker) under peak force tapping (PFT) feedback and intermittently indents on the sample surface. The PFT frequency (1kHz) is routed from the AFM controller and converted into a TTL waveform of the same frequency by a phase-lock-loop from a lock-in amplifier (MFLi, Zurich Instruments). The same TTL waveform triggers a quantum cascade laser (MIRcat-QT, DRS Daylight Photonics) to emit a train of mid-infrared laser pulses, as the PFIR signal can be enhanced by using multiple laser pulses.[30] The timing of the laser is adjusted by the phase-lock-loop so that the laser emission is synchronized with every PFT cycle when the tip is dynamically indented on the sample surface (the first pulse arrives at the peak force setpoint). Laser pulses from the QCL are steered towards the TIR prism made of germanium to create an evanescent field with an incident angle of 20°. The field confinement underneath the AFM tip excites the sample placed at the surface of the prism, causing photothermal expansions at the moment of tip-

sample dynamic contact in the PFT cycle. The repetition rate of laser pulses is adjusted to match one of the cantilever's contact resonant frequencies. The AFM tip mechanically detects the photothermal expansion through the vertical deflection of the AFM cantilever, which is measured by the deflection of a diode laser bouncing off the reflective surface of the cantilever.

Because the laser source emits pulses at every PFT cycle, all cantilever deflection traces contain responses with photothermal expansions. To extract the signal from a slow varying background of cantilever deflection, a smooth background from the 4$^{th}$ order polynomial fit is subtracted from the PFT trace, as shown in Figure 1d. The resulting oscillations of the cantilever are shown in Figure 1e, and the amplitude of these oscillations is extracted by fast Fourier Transform (FFT, Figure 1e inset). In our implementation, we use the amplitude of laser-induced cantilever oscillations to represent the photothermal expansions, which are proportional to local infrared absorptions.

**Experimental parameters of TIR-PFIR apparatus.** The apparatus shown in Figure 1c was used for both TIR-PFIR and TIR-PiFM. In the TIR-PFIR measurements of PS:PMMA blend samples, a gold-coated tip (HQ:NSC19/Cr-Au, MikroMasch) and a laser repetition rate of 208 kHz was used. The signal was from the FFT peak at 208 kHz. In the TIR-PFIR measurements of PS-b-PMMA copolymer samples, a gold-coated tip (HQ:NSC14/Cr-Au, MikroMasch) and a laser repetition rate of 186 kHz was used. The signal was from FFT peaks at 186 or 372 kHz. For the *h*-$^{10}$BN sample, the same gold-coated tip and a laser repetition rate of 440 kHz was used. The signal was from FFT peaks at 440 kHz. Detailed configurations of PiFM are described in the results section later.

**Preparation of PS:PMMA blend polymer and PS-b-PMMA copolymer samples**. Polystyrene (PS, Mw: 192000, Sigma-Aldrich) and polymethyl methacrylate (PMMA, Mw: 120000, Sigma-Aldrich) were dissolved in toluene to form a 12 mg/mL solution (the weight ratio of PS:PMMA is 1:1.5). Then, the blend polymer sample was made by spin-coating 50 µL of the solution onto a 3-cm$^2$ top surface of Ge prism at 2500 rpm for 1 min by a spin-coat machine (KW-4A, MicroNano Tools) and a customized adaptor for the prism. PS-b-PMMA (PS Mw: 96500 and PMMA Mw: 35500, Polymer Source) was dissolved in toluene to form a 10 mg/mL solution, and 50 µL of it was spin-coated on a Ge prism top surface at 1500 rpm for 1 min. Thickness of the film was measured using AFM in supplementary Fig. S1.

**Preparation of *h*-$^{10}$BN samples.** The *h*-$^{10}$BN crystals were grown from a molten metal solution, via a method similar to that reported by Liu *et al*.[31] It consisted of a two-step process: ingot formation and crystal growth. In the ingot formation step, a 50 g mixture of powdered boron and iron (2.15 mass% B-10 with balance iron) was placed in an alumina boat, then inserted into an alumina tube furnace. This was purged with nitrogen to remove oxygen, then a $N_2/H_2$ mixture (11% $H_2$) was flowed through the tube for the duration of the experiment. Next, the furnace was heated to 1550°C and held there for 24 hours to ensure the materials melted and mixed well, then quenched back to room temperature. For the crystal growth step, the ingot formed in the first step was reinserted in the furnace, which was purged using the same procedure as in the first step, then held at 1550 °C for 24 hours with the same $N_2/H_2$ mixture to saturate the solution with nitrogen. Next, the system was slowly cooled at 1°C/hour to cause *h*-$^{10}$BN to precipitate, then quenched once it reached 1500 °C. The resulting ingot was covered in a thin layer of crystals, which were peeled off with thermal release tape to produce the free-standing flakes used in this study. The *h*-$^{10}$BN flake used in this study was exfoliated onto the Ge prism top surface by a scotch tape (Scotch Magic Tape). The top surface was rinsed with acetone before use.

**Results and Discussion**

The TIR-PFIR is demonstrated on several representative samples. Figure 2 shows results from a phase-separated polymer blend sample composed of polystyrene (PS) and polymethyl methacrylate (PMMA). AFM topography of the PS:PMMA blend sample is shown in Figure 2a. A clear height difference between higher circular islands and lower matrix is observed, which reveals the nanoscale phase separation of two polymers. To determine which domains are more enriched with PS, the laser frequency is tuned to 1493 cm$^{-1}$ corresponding to aromatic C=C stretching vibrations of PS. The resulting TIR-PFIR image is shown in Figure 2c, where the lower matrix is highlighted, indicating the matrix is PS-enriched. On the other hand, the TIR-FTIR image at 1725 cm$^{-1}$ that is absorbed strongly by C=O groups (Figure 2d) selectively highlights the higher islands, indicating those islands are PMMA-enriched.

To rule out possible systematic errors, the laser is tuned to 1640 $cm^{-1}$, at which the laser intensity is strongest among three frequencies but neither PS nor PMMA is absorbing, and the tip is scanned over the same area again to obtain a background image as shown in Figure 2b. Slight artifacts around edges of islands are observed, but overall both islands and matrix show the same signal as expected. These results demonstrate that the TIR-PFIR is sensitive to nanoscale chemical compositions like the regular PFIR. Spectra measurements are conducted by parking the AFM tip at a fixed location of the sample surface while sweeping the laser frequency. Spectra from PMMA-rich and PS-rich domains are shown in Figure 2e, where infrared fingerprints are identified for each polymer. The TIR-PFIR spectrum of PMMA clearly resolves a strong carbonyl C=O absorbing peak, along with peaks at around 1150, 1270 (both are from C-O-C stretching), 1380 (α-methyl group vibration), and 1445 $cm^{-1}$ (methyl C-H vibrations). In contrast, the PS-rich domain's spectrum clearly shows aromatic C=C vibrations at 1450, 1495 and 1601 $cm^{-1}$. Note that there are several peaks (e.g. 1725 $cm^{-1}$) present in both spectra, which may be caused by underlaying PMMA or PS components.

To estimate the spatial resolution of TIR-PFIR, a PS-b-PMMA diblock copolymer sample with the nanoscale domain size of 20-30 nm is measured (Figure 3). The topography, TIR-PFIR images at 1493 and 1725 $cm^{-1}$ are shown in Figure 3a to Figure 3c. Spatial complimentary responses of the diblock copolymers are observed for PS and PMMA domains. Analysis of the spatial resolution is performed through two-dimensional Fourier transform of the image (Figure 3d). The central region of the spatial frequencies are integrated to form a profile in spatial frequency domain (Figure 3e). The bandwidth of the spatial frequency (0.1 $nm^{-1}$) is used to estimate the spatial resolution, which corresponds to an effective spatial resolution of 10 nm on this measurement. Note that the spatial resolution here is limited by the relatively high noise in our TIR-PFIR image, possibly due to the high mechanical noise of the AFM (Bioscope Catalyst, Bruker). In our previous PFIR microscopy demonstrations, a low-noise AFM (Multimode 8, Bruker) was used and a higher resolution of 6 nm was obtained. [24]

Hyperbolic boron nitride (*h*-BN) is one of the polar two-dimensional materials that support mid-infrared phonon polaritons.[32] Photothermal expansions are also used as a tool to map plasmonic responses and phonon polaritons.[26, 30, 33] Here, we used an isotopically pure *h*-$^{10}$BN flake as the sample to demonstrate that TIR-PFIR can also map the optical near-field of phonon polaritons. Figure 4 displays TIR-PFIR results on a 56-nm thick *h*-$^{10}$BN flake; its topography is shown in Figure 4a. TIR-PFIR Images at three representative frequencies of 1415, 1425 and 1435 $cm^{-1}$ are shown in Figure 4b-d, where fringe patterns of phonon polaritons parallel to the sample edge are present. These results demonstrate that although the sample surface is 56-nm away from the Ge/air interface, the tip-enhancement from the TIR evanescent field is still strong enough to launch phonon polaritons. The periodicity of those fringes can be extracted by integrating the image along the vertical direction and is shown in Figure 4e. As laser frequency increases, the periodicity of phonon polaritons decreases because polaritons with high momentum are increasingly coupled and excited. After multiple TIR-PFIR measurements at a series of laser frequencies, the dispersion relation of *h*-$^{10}$BN phonon polaritons is extracted and plotted in Figure 4f. The fringe patterns disappear below 1405 $cm^{-1}$. At laser frequencies lower than 1405 $cm^{-1}$, the whole *h*-$^{10}$BN flake exhibits a constant IR absorbing signal that is mainly from the phonon absorption. Figure 4g illustrates the spectra obtained from 5 locations from the sample edge with 500-nm intervals, all of them show a single broad peak around 1392 $cm^{-1}$, which agree well with the phonon mode of *h*-$^{10}$BN at 1394.5 $cm^{-1}$ reported in literature.[34] One can estimate a spatial resolution of 10 nm from the TIR-PFIR signal across the sharp edge of *h*-$^{10}$BN, as shown in Figure 4h.

Since the tip-enhancement in the TIR configuration is proved to be efficient experimentally, as an extension of TIR geometry for nano-IR microscopy, we also implemented the PiFM with TIR geometry. PiFM is another nano-IR method that delivers high spatial resolution (< 10 nm) infrared imaging.[25, 35] Also known as tapping AFM-IR,[36] PiFM uses tapping mode AFM feedback, thus it is less likely to damage the sample surface than contact mode PTIR method. The transition from TIR-PFIR to TIR-PiFM is accomplished by changing the working mode of AFM to the tapping mode from the PFT mode. A cantilever (HQ:NSC14/Cr-Au, MikroMasch) with two well-defined mechanical resonances ($\Omega_1$=151 kHz, $\Omega_2$=984 kHz) is used. The tapping mode feedback is on the second mechanical resonance mode $\Omega_2$. The repetition rate of the QCL laser is chosen to match the frequency difference between two mechanical resonant modes of the cantilever, which is at $\Omega_2 - \Omega_1$ (833 kHz). A lock-in amplifier (MFLi, Zurich Instruments) is used

to detect the induced cantilever oscillation at the first mechanical resonance $\Omega_1$, and the demodulation signal is used as TIR-PiFM signals.

PS:PMMA blend polymers are also investigated by the TIR-PiFM and results are shown in Figure 5. Similar to the TIR-PFIR, topography (Figure 5a), off-resonance background at 1640 $cm^{-1}$ (Figure 5b), PS-rich domains at 1493 $cm^{-1}$ (Figure 5c), PMMA-rich islands at 1725 $cm^{-1}$ (Figure 5d) and spectra collected at two domains (Figure 5e) are obtained. As a result, the feasibility of TIR-PiFM configuration is demonstrated, although in the tapping mode the tip is only close to the sample surface for a short period.

One of advantages of the TIR geometry over the regular side illumination is the easiness of optical alignment. In the regular PFIR and other nano-IR microscopies, the side illumination requires the laser beam to be exactly aligned to the tip-sample region. The illumination on the AFM cantilever has to be minimized, because photothermal induced mechanical effect will cause the AFM cantilever to oscillate, even in the absence of the sample that contains infrared resonance. Such non-resonant cantilever response from stray illumination introduces background in signals of action-based AFM infrared microscopy. As a result, tight focus and careful optical alignment is needed for side illumination nano-IR microscopy. On the other hand, the short-range evanescent field of the TIR geometry cannot excite the photothermal response of the AFM cantilever directly, thus avoiding the background. Moreover, the higher field enhancement of the TIR geometry means that the laser beam can be less tightly focused than the side illumination. A long focal distance lens can be used in designing the TIR-PFIR apparatus, rather than using short focal distance parabolic mirrors for the instrument. These two advantages provide flexibilities in instrument designing for AFM-based infrared microscopy, as well as reduction of maintenance for the imaging apparatus.

Another benefit of using the TIR geometry is that it opens the access to in-liquid nano-IR imaging. The mid-infrared evanescent field generated from TIR at the prism/water interface can reach several microns into the water, exciting photothermal effect of the infrared resonance in the sample, thus bypassing the strong attenuation of free-space IR propagation in the side illumination geometry for fluid phase nano-IR microscopies. The TIR-PTIR has been utilized to image polymer patterns[37] and study secondary structures of proteins in the liquid.[38] Nano-imaging of *h*-BN phonon polaritons with PFIR have also been demonstrated in water.[39] Relatively, in-liquid s-SNOM has also been demonstrated in water for the chemical identification through the TIR geometry using either a ZnSe prism[19] or a silicon-made solid immersion lens.[20]

**Conclusions**

In conclusion, we have demonstrated both PFIR microscopy and PiFM in the total internal reflection geometry. The development improves the spatial resolution of TIR-IR microscopy to 10 nm from the existing 50-100 nm of the PTIR in the total internal reflection geometry. Further development of the TIR-PFIR provide a route toward infrared nano imaging in the fluid phase application.

## ACKNOWLEDGMENT

X. G. X. would like to thank the support from Beckman Young Investigator Award from the Arnold and Mabel Beckman Foundation and the Sloan Research Fellowship from the Alfred P. Sloan Foundation. H. W. and X.G.X. would like to thank the support from the National Science Foundation, award number CHE 1847765. Support for the *h*-BN crystal growth from the Office of Naval Research award N00014-20-1-2474 is greatly appreciated by E. J. and J. E.

## SUPPORTING INFORMATION

The Supporting Information is available free of charge on the ACS Publications website.

Figure S1. Polymer thickness measurements.

## CONFLICT of INTEREST DISCLOSURE

The authors declare no conflict of interest.

## REFERENCES

1. Rintoul, L.; Davis, B. A.; Moghaddam, A., The unintentional excitation of surface phonon polaritons in ATR-FTIR spectra of geological samples. *Vib. Spectrosc.* **2020,** *107*, 103043.
2. Chan, K. A.; Gulati, S.; Edel, J. B.; de Mello, A. J.; Kazarian, S. G., Chemical imaging of microfluidic flows using ATR-FTIR spectroscopy. *Lab Chip* **2009,** *9* (20), 2909-2913.

3. Gok, S.; Severcan, M.; Goormaghtigh, E.; Kandemir, I.; Severcan, F., Differentiation of Anatolian honey samples from different botanical origins by ATR-FTIR spectroscopy using multivariate analysis. *Food Chem.* **2015,** *170*, 234-240.
4. Chan, K. A.; Hammond, S. V.; Kazarian, S. G., Applications of attenuated total reflection infrared spectroscopic imaging to pharmaceutical formulations. *Anal. Chem.* **2003,** *75* (9), 2140-2146.
5. Lu, R.; Li, W.-W.; Katzir, A.; Raichlin, Y.; Mizaikoff, B.; Yu, H.-Q., Fourier transform infrared spectroscopy on external perturbations inducing secondary structure changes of hemoglobin. *Analyst* **2016,** *141* (21), 6061-6067.
6. Kazarian, S.; Chan, K., Applications of ATR-FTIR spectroscopic imaging to biomedical samples. *Biochim. Biophys. Acta, Biomembr.* **2006,** *1758* (7), 858-867.
7. Mojet, B. L.; Ebbesen, S. D.; Lefferts, L., Light at the interface: the potential of attenuated total reflection infrared spectroscopy for understanding heterogeneous catalysis in water. *Chem. Soc. Rev.* **2010,** *39* (12), 4643-4655.
8. Ortiz-Hernandez, I.; Williams, C. T., In situ investigation of solid− liquid catalytic interfaces by attenuated total reflection infrared spectroscopy. *Langmuir* **2003,** *19* (7), 2956-2962.
9. Ferri, D.; Bürgi, T., An in situ attenuated Total reflection infrared study of a chiral catalytic solid− liquid Interface: Cinchonidine adsorption on Pt. *J. Am. Chem. Soc.* **2001,** *123* (48), 12074-12084.
10. Abbe, E., Beiträge zur Theorie des Mikroskops und der mikroskopischen Wahrnehmung. *Archiv für mikroskopische Anatomie* **1873,** *9* (1), 413-418.
11. Chan, K.; Kazarian, S., New opportunities in micro-and macro-attenuated total reflection infrared spectroscopic imaging: spatial resolution and sampling versatility. *Appl. Spectrosc.* **2003,** *57* (4), 381-389.
12. Kazarian, S. G.; Chan, K. A., ATR-FTIR spectroscopic imaging: recent advances and applications to biological systems. *Analyst* **2013,** *138* (7), 1940-1951.
13. Dazzi, A.; Prazeres, R.; Glotin, F.; Ortega, J., Local infrared microspectroscopy with subwavelength spatial resolution with an atomic force microscope tip used as a photothermal sensor. *Opt. Lett.* **2005,** *30* (18), 2388-2390.
14. Lahiri, B.; Holland, G.; Centrone, A., Chemical imaging beyond the diffraction limit: experimental validation of the PTIR technique. *Small* **2013,** *9* (3), 439-445.
15. Ramer, G.; Aksyuk, V. A.; Centrone, A., Quantitative chemical analysis at the nanoscale using the photothermal induced resonance technique. *Anal. Chem.* **2017,** *89* (24), 13524-13531.
16. Knoll, B.; Keilmann, F., Near-field probing of vibrational absorption for chemical microscopy. *Nature* **1999,** *399* (6732), 134-137.
17. Aubert, S.; Bruyant, A.; Blaize, S.; Bachelot, R.; Lerondel, G.; Hudlet, S.; Royer, P., Analysis of the interferometric effect of the background light in apertureless scanning near-field optical microscopy. *J. Opt. Soc. Am. B* **2003,** *20* (10), 2117-2124.
18. Hudlet, S.; Aubert, S.; Bruyant, A.; Bachelot, R.; Adam, P.-M.; Bijeon, J.-L.; Lérondel, G.; Royer, P.; Stashkevich, A. A., Apertureless near field optical microscopy: a contribution to the understanding of the signal detected in the presence of a background field. *Opt. Commun.* **2004,** *230* (4), 245-251.
19. O'Callahan, B. T.; Park, K.-D.; Novikova, I. V.; Jian, T.; Chen, C.-L.; Muller, E. A.; El-Khoury, P. Z.; Raschke, M. B.; Lea, A. S., In Liquid Infrared Scattering Scanning Near-Field Optical Microscopy for Chemical and Biological Nanoimaging. *Nano Lett.* **2020,** *20* (6), 4497-4504.
20. Pfitzner, E.; Heberle, J., Infrared Scattering-Type Scanning Near-Field Optical Microscopy of Biomembranes in Water. *J. Phys. Chem. Lett.* **2020,** *11* (19), 8183-8188.
21. Huth, F.; Govyadinov, A.; Amarie, S.; Nuansing, W.; Keilmann, F.; Hillenbrand, R., Nano-FTIR Absorption Spectroscopy of Molecular Fingerprints at 20 nm Spatial Resolution. *Nano Lett.* **2012,** *12* (8), 3973-3978.
22. Ocelic, N.; Huber, A.; Hillenbrand, R., Pseudoheterodyne detection for background-free near-field spectroscopy. *Appl. Phys. Lett.* **2006,** *89* (10), 101124.
23. Xu, X. G.; Tanur, A. E.; Walker, G. C., Phase Controlled Homodyne Infrared Near-Field Microscopy and Spectroscopy Reveal Inhomogeneity within and among Individual Boron Nitride Nanotubes. *J. Phys. Chem. A* **2013,** *117* (16), 3348-3354.
24. Katzenmeyer, A. M.; Holland, G.; Kjoller, K.; Centrone, A., Absorption spectroscopy and imaging from the visible through mid-infrared with 20 nm resolution. *Anal. Chem.* **2015,** *87* (6), 3154-3159.
25. Nowak, D.; Morrison, W.; Wickramasinghe, H. K.; Jahng, J.; Potma, E.; Wan, L.; Ruiz, R.; Albrecht, T. R.; Schmidt, K.; Frommer, J., Nanoscale chemical imaging by photoinduced force microscopy. *Sci. Adv.* **2016,** *2* (3), e1501571.
26. Wang, L.; Wang, H.; Wagner, M.; Yan, Y.; Jakob, D. S.; Xu, X. G., Nanoscale simultaneous chemical and mechanical imaging via peak force infrared microscopy. *Sci. Adv.* **2017,** *3* (6), e1700255.
27. Hecht, E., *Optics*. Pearson Education, Incorporated: 2017.
28. Milosevic, M., On the nature of the evanescent wave. *Appl. Spectrosc.* **2013,** *67* (2), 126-131.
29. Tanabe, K., Field enhancement around metal nanoparticles and nanoshells: a systematic investigation. *J. Phys. Chem. C* **2008,** *112* (40), 15721-15728.
30. Wang, L.; Wagner, M.; Wang, H.; Pau ‐ Sanchez, S.; Li, J.; Edgar, J. H.; Xu, X. G., Revealing Phonon Polaritons in Hexagonal Boron Nitride by Multipulse Peak Force Infrared Microscopy. *Adv. Opt. Mater.* **2019**, 1901084.
31. Liu, S.; He, R.; Xue, L.; Li, J.; Liu, B.; Edgar, J. H., Single Crystal Growth of Millimeter-Sized Monoisotopic Hexagonal Boron Nitride. *Chem. Mater.* **2018,** *30* (18), 6222-6225.
32. Dai, S.; Fei, Z.; Ma, Q.; Rodin, A.; Wagner, M.; McLeod, A.; Liu, M.; Gannett, W.; Regan, W.; Watanabe, K., Tunable phonon polaritons in atomically thin van der Waals crystals of boron nitride. *Science* **2014,** *343* (6175), 1125-1129.
33. Brown, L. V.; Davanco, M.; Sun, Z.; Kretinin, A.; Chen, Y.; Matson, J. R.; Vurgaftman, I.; Sharac, N.; Giles, A. J.; Fogler, M. M., Nanoscale mapping and spectroscopy of nonradiative hyperbolic modes in hexagonal boron nitride nanostructures. *Nano Lett.* **2018,** *18* (3), 1628-1636.
34. Giles, A. J.; Dai, S.; Vurgaftman, I.; Hoffman, T.; Liu, S.; Lindsay, L.; Ellis, C. T.; Assefa, N.; Chatzakis, I.; Reinecke, T. L., Ultralow-loss polaritons in isotopically pure boron nitride. *Nat. Mater.* **2018,** *17* (2), 134-139.

35. Wang, L.; Jakob, D. S.; Wang, H.; Apostolos, A.; Pires, M. M.; Xu, X. G., Generalized Heterodyne Configurations for Photoinduced Force Microscopy. *Anal. Chem.* **2019,** *91* (20), 13251-13259.
36. Wieland, K.; Ramer, G.; Weiss, V. U.; Allmaier, G.; Lendl, B.; Centrone, A., Nanoscale chemical imaging of individual chemotherapeutic cytarabine-loaded liposomal nanocarriers. *Nano Res.* **2019,** *12* (1), 197-203.
37. Jin, M.; Lu, F.; Belkin, M. A., High-sensitivity infrared vibrational nanospectroscopy in water. *Light: Sci. Appl.* **2017,** *6* (7), e17096-e17096.
38. Ramer, G.; Ruggeri, F. S.; Levin, A.; Knowles, T. P. J.; Centrone, A., Determination of Polypeptide Conformation with Nanoscale Resolution in Water. *ACS Nano* **2018,** *12* (7), 6612-6619.
39. Wang, H.; Janzen, E.; Wang, L.; Edgar, J. H.; Xu, X. G., Probing Mid-Infrared Phonon Polaritons in the Aqueous Phase. *Nano Lett.* **2020,** *20* (5), 3986-3991.

**Graphics**

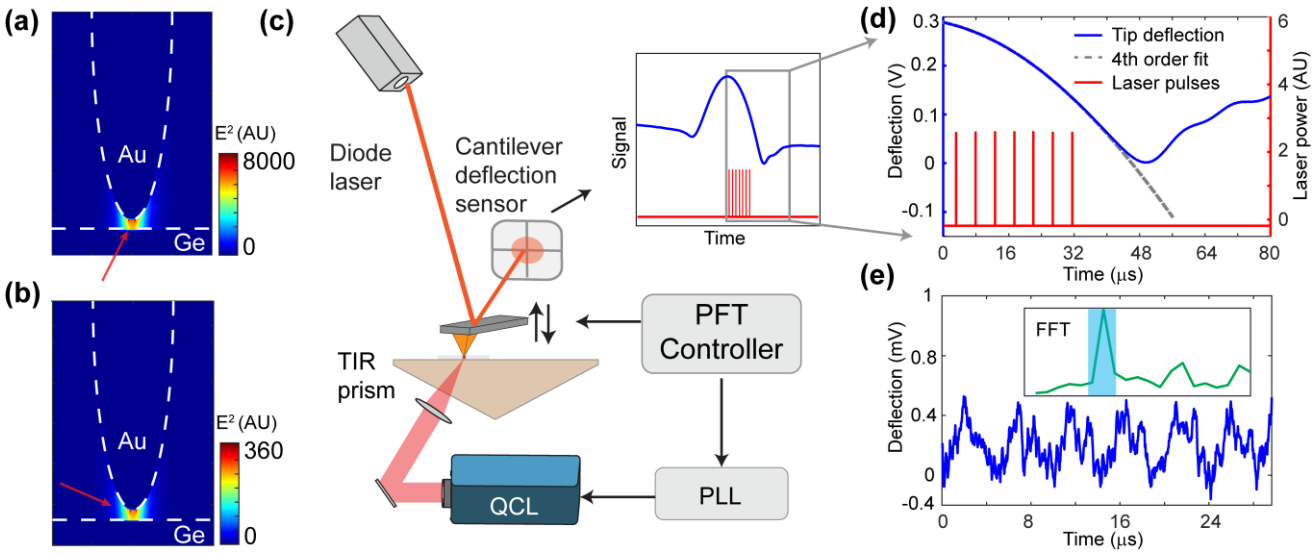


**Figure 1.** FDTD simulations of TIR and TIR-PFIR mechanism. (a) FDTD simulation of the field enhancement of a metallic AFM tip by evanescent field from a total internal reflection of a Ge prism. The tip is represented by a Au cone with an end radius of 30 nm. A P-polarized plane wave (polarized in the image plane) with the frequency of 1390 $cm^{-1}$ is used as the light source, the incident angle is 20° as the red arrow shows. (b) FDTD simulation of field enhancement of a Au tip by direct illumination from the side, the incident angle is 15° with respect to the horizontal axis. (c) Schematics of the TIR-PFIR apparatus. The graph on the upper right corner schematically shows a full PFT cycle with cantilever deflection (blue) and laser pulses (red). (d) Cantilever deflection traces with oscillations caused by photothermal expansions (blue) and fitted background (dashed gray). The timing of the laser pulses is shown as the red curve. (e) Extracted tip oscillations from (d). The oscillations are induced by a train of pulses of 1725 $cm^{-1}$ with the repetition rate of 208 kHz, when tip is parked on the PMMA sample. The area of the first peak at 208 kHz in the FFT result (shown in inset) is used as TIR-FTIR signal.

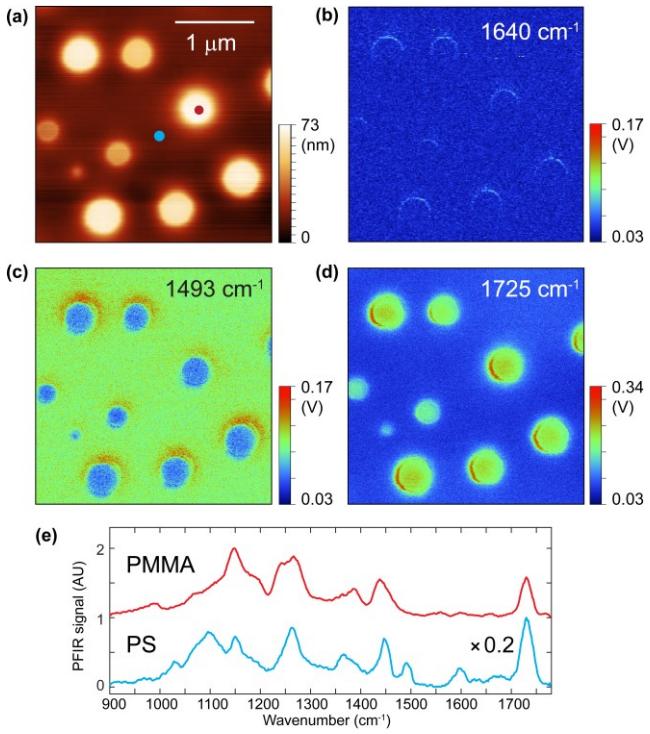


**Figure 2.** TIR-PFIR measurements on phase separated PS:PMMA blend polymers. (a) Topography of PS:PMMA blend sample. (b) TIR-PFIR image at 1640 $cm^{-1}$. (c) TIR-PFIR image at 1493 $cm^{-1}$, where PS-rich domains show stronger signals. (d) TIR-PFIR image at 1725 $cm^{-1}$, where PMMA-rich domains show stronger signals. (e) Point spectra collected at PS-rich and PMMA-rich domains. Measuring locations are labelled as cyan and red dots in (a) for PS and PMMA-rich domains, respectively. The laser power within 1450-1780 $cm^{-1}$ range in the spectrum of PMMA is reduced to 1/5 of that of the spectrum of PS, in order to avoid melting sample.

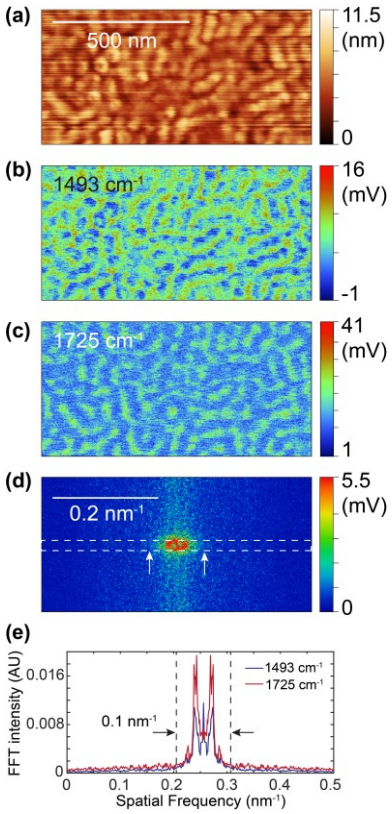


**Figure 3.** TIR-PFIR on the diblock copolymer and the estimation of the spatial resolution. (a) Topography of the PS-b-PMMA diblock copolymer. (b) TIR-PFIR image with the infrared frequency of 1493 $cm^{-1}$, which is on resonance with the PS domain. (c) TIR-PFIR image with the infrared frequency of 1725 $cm^{-1}$, which is on resonance with the PMMA domain. (d) Two-dimensional Fourier transform (2DFFT) of (b). Two white arrows indicate the bandwidth of the spatial frequency. (e) Averaged profiles of 2DFFT maps of (b-c). The area of averaging is marked as a dashed white box in (d). An effective spatial resolution of 10 nm can be estimated from the bandwidth of the spatial frequency (0.1 $nm^{-1}$) on the measurement of PS-b-PMMA copolymer film. The complex central features of the profile are from the overall phase separation in space.

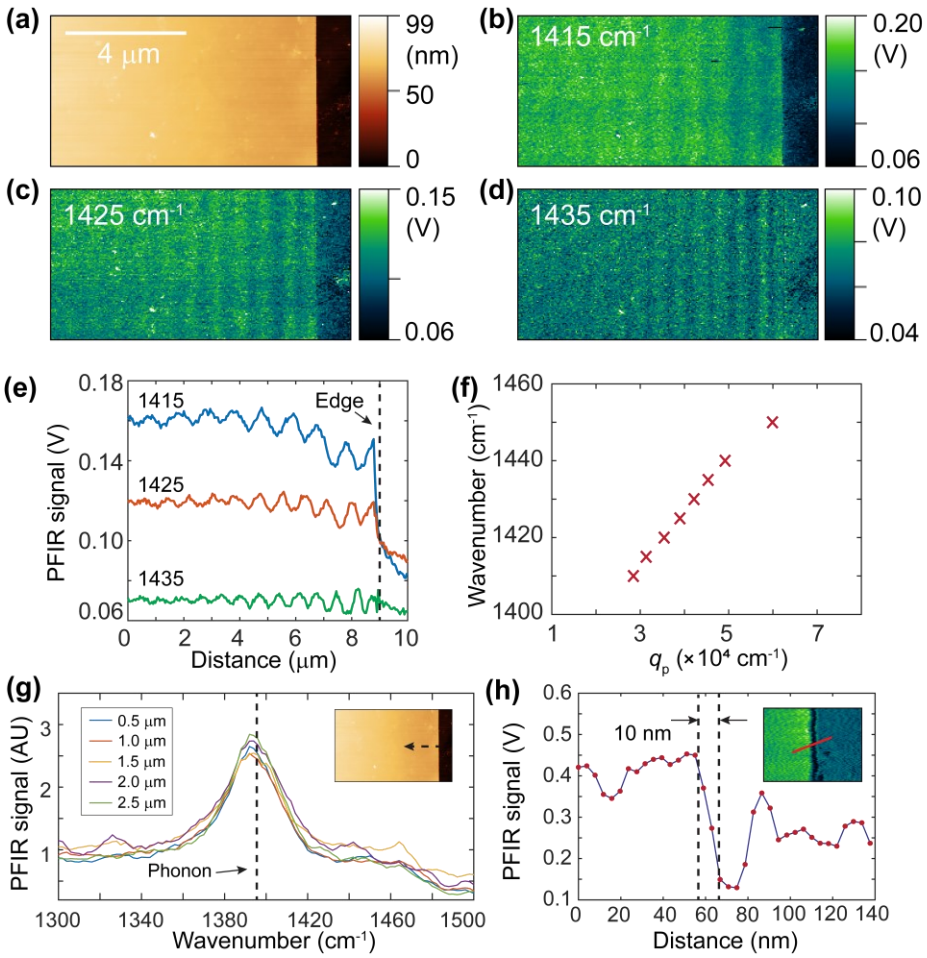


**Figure 4.** TIR-PFIR measurements on an *h*-$^{10}$BN flake. (a) Topography of the *h*-$^{10}$BN flake. (b-d) TIR-PFIR images at 1415, 1425 and 1435 cm$^{-1}$, respectively. Fringe patterns caused by the transportation of phonon polaritons are noticeable. (e) Fringe patterns extracted from (b-d). The location of sample edge is indicated by a dashed black line. (f) Experimental dispersion relation of *h*-$^{10}$BN phonon polaritons. (g) TIR-PFIR spectra collected at five locations with 500-nm intervals along the arrows shown in the inset. The first location is 500 nm from the edge. The phonon mode from the literature is shown by a dashed black line. (h) Cross section of TIR-PFIR signals along the *h*-$^{10}$BN edge. Inset shows a high-resolution TIR-PFIR image at 1390 cm$^{-1}$, and the cross-sectioning locations is marked by a red line.

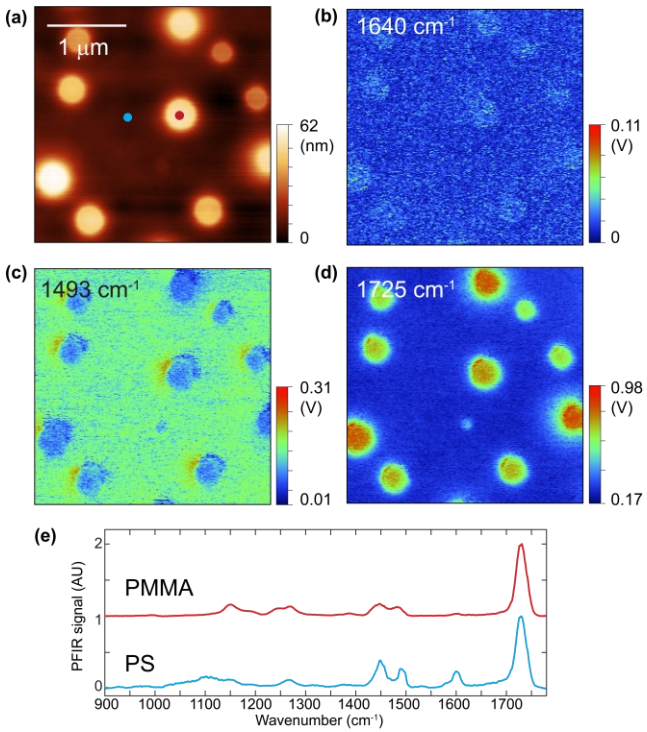


**Figure 5.** TIR-PiFM measurements on phase separated PS:PMMA blend polymers. (a) Topography of PS:PMMA blend sample. (b) TIR-PiFM image at 1640 $cm^{-1}$. (c) TIR-PiFM image at 1493 $cm^{-1}$, where PS-rich domains show stronger signals. (d) TIR-PiFM image at 1725 $cm^{-1}$, where PMMA-rich domains show stronger signals. (e) Point spectra collected at PS-rich and PMMA-rich domains. Measuring locations are labeled as cyan and red dots in (a) for PS and PMMA-rich domains, respectively.

ToC figure